Growth, Electronic Structure, and Electrochemical Properties of Cubic BaTiO₃ Synthesized by Low-Pressure Hydrothermal-Assisted Sintering

Mohammad Khotib[1,2*], Bambang Soegijono[3], Zainal Alim Mas'ud[1,2], and Gina Libria Nadjamoeddin[2]

[1]Department of Chemistry, Bogor Agricultural University, Chemistry Building, Wing 1, 3rd Floor,
Jl. Tanjung, IPB Darmaga Campus, Bogor 16680, Indonesia

[2]Laboratory for Testing, Calibration and Certification Services, Bogor Agricultural University, Baranangsiang Campus,
Jl. Padjajaran, Bogor 16129, Indonesia

[3]Department of Physics, Faculty of Mathematics and Natural Sciences, Universitas Indonesia,
Kampus Baru UI, Depok 16424, Indonesia

Abstract: *Cubic BaTiO₃ was synthesized through low-pressure hydrothermal-assisted sintering using Ba(OH)₂ and TiO₂ as precursors with a mol ratio of Ba:Ti = 1.4:1. The single phase of cubic BaTiO₃ was produced at a sintering temperature of 800 °C for 2, 4, 8, and 12 h. The absence of diffraction peak splitting at 2θ of 45° was indicated cubic BaTiO₃. The crystallite size of BaTiO₃ ranged from 80–200 nm, and its size increased with increasing temperatures and sintering times. The micro-strain of the BaTiO₃ crystal lattice had a range between 0.27 and 0.68%. The minimum bandgap on the indirect bandgap was about 1.75 eV from point M to Γ, while the direct bandgap was about 1.95 eV from Γ to Γ. Ti–O's interaction had a covalent character, while that of Ba–O had an ionic character based on the density of state (DOS) calculation. The characteristics of the BaTiO₃ voltammogram show an irreversible redox mechanism with a more observable reduction peak in Ti⁴⁺/Ti³⁺. Higher current density at over potential indicated greater BaTiO₃ capabilities in Oxygen Evolution Reaction (OER)-Oxygen Reduction Reaction (ORR) electrocatalysis. For that, purified cubic BaTiO₃ offers potential application as an electrode for batteries, water splitting systems, and regenerative fuel cells.*

Keywords: cubic BaTiO₃; bandgap; the density of state; oxygen evolution-reduction; electrocatalyst

■ INTRODUCTION

Barium titanate (BaTiO₃) is widely used as the main material for multilayer capacitors, thermistors, high-density data storage, and electro-optical equipment due to its dielectric and ferroelectric properties as well as environmentally friendly materials. The application of BaTiO₃ to electronic materials is closely related to the character of its microstructures. The nano-size of BaTiO₃ also exhibits better performance than other sizes. BaTiO₃ is also known to have abilities in the electrolysis of oxygen evolution reaction (OER), oxygen reduction reaction (ORR), and hydrogen evolution reaction (HER) [1-2]. Furthermore, it is well-known that a high specific area could increase its catalytic activity by enabling a shorter

diffusion distance of its electrons and holes, facilitating the surface redox reaction. Therefore, many studies have been developed to obtain BaTiO₃ with microstructure and morphology matching application requirements.

The conventional technique of BaTiO₃ synthesis requires high temperatures (~1200 °C) followed by grinding or milling its precursors such as BaO and TiO₂ [3]. A disadvantage of this solid technique is the presence of contamination and crystal growth problems during milling and calcination. New techniques are thus being continuously developed, such as sol-gel [4-5], the Pechini process [6], hydrothermal [7], and precipitation [8-9]. These techniques can be categorized as wet techniques that facilitate the crystallization of nano-size

particles at low temperatures. A synthesis technique for BaTiO₃ is required to produce nano-sized particles free of impurities and damage.

The main advantages of low-pressure hydrothermal techniques over solid-phase techniques include lower reaction temperatures and higher product purity. In addition, hydrothermal techniques no longer require thermal treatment for crystallization [10-11], so it is possible to obtain sub-micro or nano-sized materials of BaTiO₃. Crystallization via the hydrothermal technique also provides advantages over sol-gel and co-precipitation, such as shorter crystallization times with good control over crystallization, crystallite size, purity, and morphology [12].

Based on the above explanation of the many benefits of BaTiO₃ as a ferroelectric material and the advantages of the hydrothermal technique, a study was conducted to obtain cubic BaTiO₃ using a low-pressure hydrothermal technique and identify its crystal growth.

■ EXPERIMENTAL SECTION

Materials

All the reagents were obtained from PT Merck Indonesia Tbk, analytical grade, and used without further purification, i.e., $Ba(OH)_2 \cdot 8H_2O$ (for an analysis-ensure grade, Merck, Germany), TiO_2 (for an analysis-ensure grade, Merck, Germany), and HNO_3 (for analysis-65% purity, Merck, Germany).

Instrumentation

The equipment for synthesis and characterization were oven (Memmert UN55), XRD (Shimadzu XRD-7000), TG/DTA (LINSEISS STA PT 1600), and Potentiostat (Digi-Ivy).

Procedure

Synthesis of cubic barium titanate (Cubic BaTiO₃)

Cubic BaTiO₃ was synthesized using barium hydroxide ($Ba(OH)_2 \cdot 8H_2O$), titanium oxide (TiO_2), and distilled water as precursors. BaTiO₃ was synthesized via a low-pressure system hydrothermal method using the mole ratio of Ba:Ti = 1.4:1. The suspension was prepared by mixing 9 g (0.12 mol) of TiO_2 and 45 g (0.14 mol) of $Ba(OH)_2 \cdot 8H_2O$ in 250 mL of CO_2-free-distilled water in a

Teflon container. The mixture was stirred evenly and heated in an oven at 150 °C until the water evaporated entirely. Then, the solid was heated at temperatures of 600, 700, and 800 °C for the following durations: (a) for 600 °C = 6, 12, 18, and 24 h, (b) for 700 °C = 4, 8, 12, and 16 h, (c) for 800 °C = 2, 4, 8, 12 h.

The purification of BaTiO₃ was conducted by immersing it in 100 mL of 1 N HNO_3 solution followed by heating at 60 °C for one hour. Next, the solid was separated, washed with distilled water until being acid-free, and dried at 105 °C for 3 h.

Phase identification using XRD

Each product was identified for phase and crystallite size using XRD GBC EMMA software Traces 28 mA, 35 kV with Cu Kθ = 1.54056 A in the 2θ range of 10 to 90°, step size = 0.02°, and scan rate= 2°/min. An analysis of the XRD data in phase identification and refinement was conducted using HighScore Plus and FullProf software using COD and the ICDD database. The BaTiO₃ crystallite size was determined by Scherrer and Williamson-Hall equations using XRD measurement data. The equations are:

Scherrer: $B = \dfrac{K\lambda}{D \cos\theta}$

Williamson-Hall: $B = \dfrac{K\lambda}{D \cos\theta} + \eta \tan\theta$

then rearranged to B. $\cos\theta = \dfrac{K\lambda}{D} + \eta \sin\theta$

where B = FWHM peaks after correction by instrumental broadening, $B = \sqrt{B_0{}^2 - B_i{}^2}$; B_0 = FWHM sample, B_i = FWHM standard (silicon), D = crystallite size, K = constant Scherrer (0.94 for cubic system), and η=strain. The sizes of the crystallite and strain were determined by making the linear equation between B*$\cos\theta$ and $\sin\theta$. The intercept and slope of the linear equations were used to determine the size of the crystal (D) and the strain of a micro-crystal lattice, respectively. The determination of crystal size through the Scherrer equation used FWHM from peaks 111 and 200 because it was close to the standard of the silicon peak [13].

Study of crystal growth

The kinetics of BaTiO₃crystal growth was determined using a Burke-Turnbull equation modification based on an isothermal reaction model:

$D_t^n - D_0^n = Ate^{-\frac{Ea}{RT}}$; this equation was rearranged to: $\ln D_t = \frac{1}{n}\ln t + \frac{1}{n}(\ln A - \frac{Ea}{RT})$ and then rearranged to: $\ln\frac{D_t^n}{t} = \ln A - \frac{Ea}{RT}$

D_t and D_0 are average grain sizes at time t and original grain size, n is the grain growth exponent, t is the sintering time, E_a is the grain growth activation energy, and A is the pre-exponential, and R is the general gas constant.

Thermal and electrochemical characteristics

The thermal properties of a low-pressure hydrothermal product prior to sintering were monitored using a TG-DTA pattern in air and oxygen atmospheric with a flow rate of 10 °C/min. In addition, the electrochemical properties of $BaTiO_3$ were obtained from cyclic voltammetry (CV) and linear sweep voltammetry (LSV). CV was performed using potentiostat DY 2300 digi-ivy, SPCE DS-110 as substrate of $BaTiO_3$, potential range (-1)–(1) V, scan rate 0.05 V/sec, and sensitivity 10^{-3} A/V in a 1 M NaOH solution.

■ RESULTS AND DISCUSSION

Cubic Barium Titanate

The single-phase was successfully synthesized through low-pressure hydrothermal at 150 °C and sintering at 800 °C for 2, 4, 8, and 12 h based on the XRD measurements (Suppl. 1–3). The $BaTiO_3$ diffractions show peaks at 2θ close to $BaTiO_3$ in the COD database No. 96-210-0863 (Fig. 1). The temperatures of the sintering and distilled water purity could affect the purity of $BaTiO_3$. The impurities of $BaTiO_3$ formed at sintering temperatures of between 600 and 700 °C. The impurities were caused by the reaction between $Ba(OH)_2$ and dissolved CO_2 in distilled water. The use of free-CO_2 distilled water, cleaning with Nitrogen/Argon, or washing with organic acids like formic acid can reduce impurities [7]. In this study, the purification of $BaTiO_3$ was successfully performed using nitric acid to remove $BaCO_3$, which was characterized by the absence of $BaCO_3$ peaks at 23.939, 24.335, 34.143, 42.045, and 43.035° after treatment with nitric acid (Fig. 1). The formation of $BaCO_3$ impurities indicates the weakness of the synthesis of $BaTiO_3$ through wet techniques performed at low sintering temperatures [14-15]. Inhibition of $BaCO_3$ formation is important for
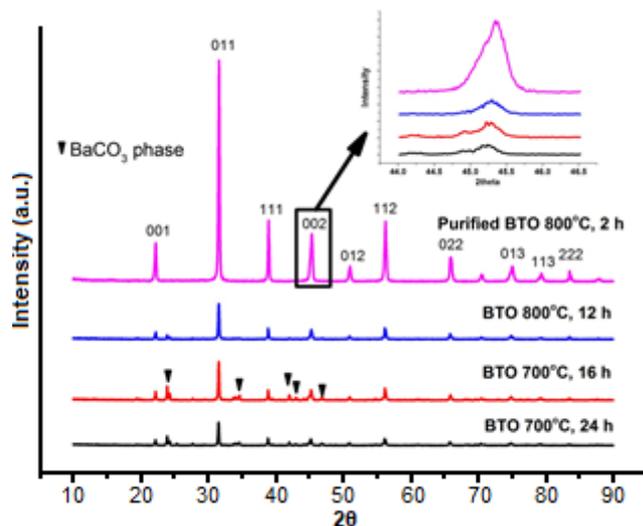
Fig 1. The XRD diffraction patterns of resulted $BaTiO_3$ using low-pressure hydrothermal assisted sintering. The black rectangular and insert shows absence splitting peak at 2θ = 45°

obtaining $BaTiO_3$ with high purity. Small amounts of $BaCO_3$ impurities were also identified in the hydrothermal synthesis of $BaTiO_3$ at 200 °C with $Ba(OH)_2$ and $TiO_2/TiCl_4$ as precursors [16].

$BaCO_3$ was also produced in synthesizing hydrothermal $BaTiO_3$, with $Ba(OH)_2$ and TiO_2 as precursors at 220 °C for three days. The impurities of the $BaCO_3$ phase decreased at the sintering temperature of 800 °C. Based on the Rietveld refinement result, the composition of $BaCO_3$ was not significantly different at 600 and 700 °C for all durations of sintering (Table 1). Moreover, the sintering temperature of 800 °C caused $BaCO_3$ to turn into BaO and CO_2.

The synthesized $BaTiO_3$ had a cubic crystal system based on the XRD diffractogram (Fig. 2), which was indicated by the absence of splitting at the diffraction peak of 2θ = 45°, the {200} plane into two peaks (i.e., {200} and {002} planes) (Fig. 1) [17-19]. Sintering at 600, 700, and 800 °C was predicted to be caused by the crystal structure change from tetragonal to cubic. Thermodynamically, $BaTiO_3$ will form a cubic crystal structure at temperatures above 130 °C.

The reaction equation and mechanism were proposed to explain the formation of $BaTiO_3$ from $Ba(OH)_2$ and TiO_2 via the hydrothermal technique.

Table 1. Phase composition in barium titanate synthesis after refinement

Treatment		Phase composition (%)		Rietveld refinement (FullProf)	
Temperature (°C)	Times (h)	BaTiO$_3$	BaCO$_3$	Chi^2	Weighted average R-Bragg
600	6	61.4	38.6	1.8	20.3
	12	64.2	35.8	1.9	21.1
	18	61.4	38.6	2.0	26.8
	24	60.1	39.9	1.9	17.7
700	4	63.2	36.8	1.9	16.7
	8	65.0	35.0	1.9	21.6
	12	70.5	29.6	1.9	20.6
	16	74.4	25.6	1.7	21.1
800	2	100		1.2	15.6
	4	100		1.4	14.4
	6	100		1.3	15.4
	8	100		1.1	12.5
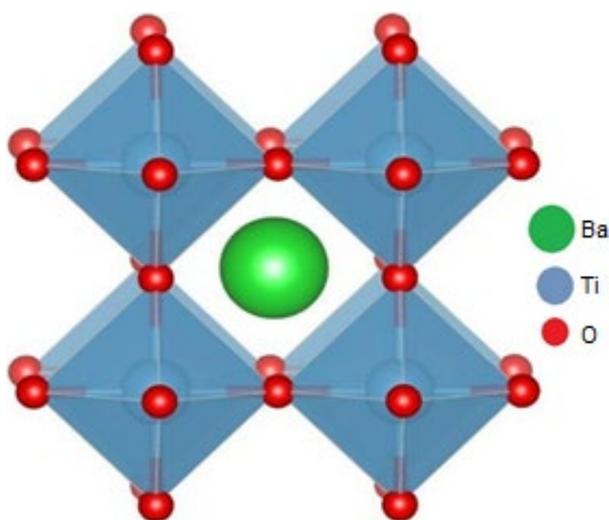
Fig 2. Crystal structure of purified cubic BaTiO$_3$

BaTiO$_3$ formation with Ba(OH)$_2$ and TiO$_2$ as precursors could be due to the dissolution-precipitation mechanism. In this mechanism, two-step reactions for BaTiO$_3$ formation were proposed [18,20]:

Dissolution: $TiO_2 + H_2O \rightarrow [Ti(OH)_{4-x}]^{x+}$

Precipitation: $[Ti(OH)_{4-x}]^{x+} + Ba^{2+} + 2\ OH^- \rightarrow BaTiO_3 + 2H_2O$
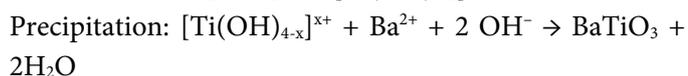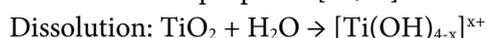
The rate of nucleation and the growth of BaTiO$_3$ were influenced by the dissolution rate of TiO$_2$, which is indicated by the surface area dependence of the resulting BaTiO$_3$ on the size of the TiO$_2$ precursor [21]. Therefore, the rate of BaTiO$_3$ formation could be increased by adding KOH or NaOH since the formation of $[Ti(OH)_{4-x}]^{x+}$ ions were accelerated in the alkaline medium. Other explanations for the formation process of BaTiO$_3$ include the condensation reaction occurring between $[Ti(OH)_6]^{2-}$ and Ba^{2+}; the migration of the Ba^{2+} ion into the TiO$_2$ structure, resulting in the breaking of Ti–O–Ti bonds; and the hydrolysis of Ti–O–Ti in an alkaline medium following the migration of the Ba^{2+} ion [22]. Thermodynamically, hydroxide ions play a role in the nucleation of BaTiO$_3$ and its function as a catalyst through the transition acceleration of Ba^{2+} ions during the dynamic point of crystallization to form BaTiO$_3$ crystals. Therefore, increasing the nucleation of BaTiO$_3$ could increase its growth and cause larger particle size.

Size and Kinetics of Crystal Growth

The crystallite size of the synthesized BaTiO$_3$ was measured using the Scherrer equation. The size of the obtained crystals ranged from 82 to 169 nm, 100 to198 nm, and 82 to149 nm for sintering temperatures of 600, 700, and 800 °C (Table 2). The crystallite size increased in line with the duration of sintering time. The crystallite size and structure of the crystal were also influenced by the particle size and TiO$_2$ precursor type, with a smaller particle size of the TiO$_2$ precursor resulting in smaller-sized BaTiO$_3$ as well. Other studies were conducted for BaTiO$_3$ hydrothermal synthesis at 96 °C with Ba (OH)$_2$ and TiO$_2$ precursors obtaining a crystallite size of 70 nm [23]. Additives, such as Polyacrylate, PVA, and fructose

Table 2. Crystallite size, rate parameter, and E_a crystal growth of cubic $BaTiO_3$

Treatments		Crystallite size (nm)	Micro-strain (η, %)	Crystal growth exponent (n)	Ea (kJ/mol)
Temperature (°C)	Time (h)				
600	6	82	0.27	2.0	119.3
	12	118	0.64		
	18	131	0.58		
	24	169	0.53		
700	4	100	0.51	2.2	
	8	134	0.59		
	12	148	0.63		
	16	198	0.53		
800	2	82	0.31	2.5	
	4	110	0.50		
	6	126	0.68		
	8	149	0.65		

to the hydrothermal process, could reduce particle size [23]. $BaTiO_3$ with a crystallite size of 75 nm (48 h of treatment) and 130 nm (72 h of treatment) were obtained using hydrothermal techniques followed by plasma spark sintering [24].

The XRD pattern could be used to calculate micro strains from the crystal lattice. One of the top causes of expansion at peak X-ray diffraction is the microstrain. $BaTiO_3$, obtained with low hydrothermal pressure at 150 °C, a sintering temperature between 600 to 800 °C, and a sintering time of 2 to 24 h has a microstrain of 0.27 to 0.68% (Table 2). Microstrains can occur due to the uniform distortion of the crystal lattice, dislocation, anti-phase domain boundaries, or deformation faulting.

The size of the crystallite material is closely related to its chemical and physical properties, so it needs to be studied to identify its crystal growth. Information on crystal growth kinetics can be used to control the desired crystal size of the material. The crystals/grains from $BaTiO_3$ growth via low-pressure hydrothermal methods were studied at sintering temperatures of 600, 700, 800 °C for different time durations. Based on the linear plot between ln (D) and ln (t) of the Burke-Turnbull equation changes, n values were 2.0, 2.2, and 2.5, respectively, for sintering temperatures 600, 700, and 800 °C. In general, the value of n ranged from 2 to 6, but there were up to 10 [24]. The exponent of crystallite growth was obtained at n

= 3.4 (matrix) and n = 9.7 (template) for the growth kinetics of the ceramic-textured $BaTiO_3$ through template techniques [25]. The greater value of n indicates the crystal growth is constrained, resulting in the slower growth of the crystal.

A correlation between the crystal growth exponent and the grain mechanism was proposed (i.e., n ≤ 3 due to pore controlled lattice diffusion, pore controlled vapor transport with constant vapor pressure, boundary controlled coalescence of the second phase particles for a system containing second phase particles, and boundary controlled solute drag for the doped system. Based on the value of the grain growth exponent, the growth mechanism of $BaTiO_3$ synthesized with low-pressure hydrothermal-assisted sintering was due to poorly controlled lattice diffusion. On the other hand, the sintering temperature change did not affect the grain growth exponent, which means that temperature changes do not affect the diffusion mechanism [26].

Crystal growth is influenced by the crystal-boundary curvature mechanism, lattice diffusion, crystal-bound diffusion, interfacial diffusion, evaporative agglomeration, the dissolving-settling mechanism, and super-saturation (concentrations of reactant, temperature, and mixing conditions) [25]. The size of the initial crystal affects the crystal formation process and its growth rate. In this research, $BaTiO_3$ had

an initial crystallite size that did not differ significantly among the materials (82 and 100 nm) and grew to 198 nm during sintering, with an activation energy of 119.8 kJ/mol (Table 2). This activation energy was in line with the growth rate. Based on our references, activation energies of 190, 202, and 196 kJ/mol for BaTiO₃ were produced using the milling technique for $BaCO_3$ and TiO_2 [27]. Activation energies of 364 kJ/mol (matrix) and 918 kJ/mol (template) for BaTiO₃ produced by the template method [25].

Electronic Structure of BaTiO₃

The bandgap and density of state (DOS) of the cubic BaTiO₃, calculated using quantum espresso with Burai as the graphical user interface (GUI), are shown in Fig. 3 and 4. For band structure, the maximum of the valence band and the minimum of the conduction band are located at the M and Γ band, respectively, with the smallest value of the direct bandgap about 1.9 eV at the Γ to Γ band and the indirect bandgap from M to Γ band being about 1.75 eV. This result was in line with Rohj et al. [28], who used DFT+U approximations for BaTiO₃ with values of 1.67 eV at the I'G band, and Taib et al. [29], who used the using LDA+U method for BaTiO₃ with a value of about 1.778 eV for the indirect bandgap. Orbital O 2p dominated the highest valence band (VB), while orbital Ti 3d dominated the lowest conduction band. Details on the electron density of cubic BaTiO₃ were explained using the DOS data.

The DOS of cubic BaTiO₃ exhibited a symmetric type (Fig. 4). The valence band (VB) from -6 to 0 eV consisted of an O 2p state with a small contribution from the Ti 3d and Ba 5p states. The conduction band minimum from 0 to 5 eV was dominated by the Ti 3d state, with a small contribution from the O 2p state, which
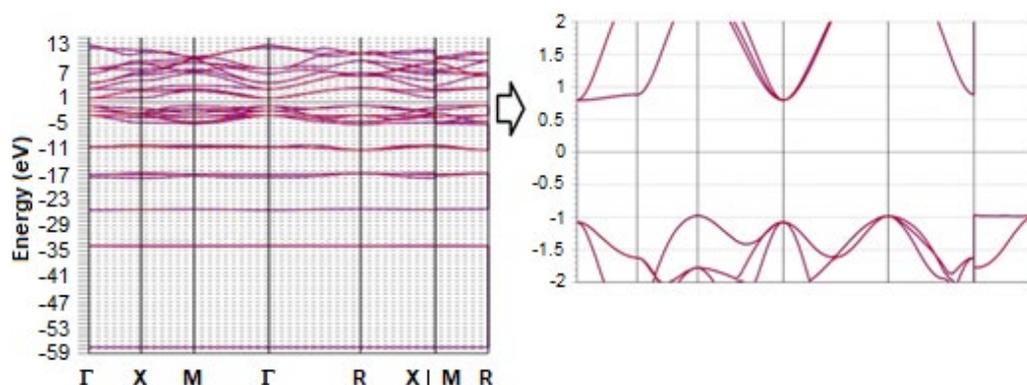
Fig 3. Band structure of cubic BaTiO₃
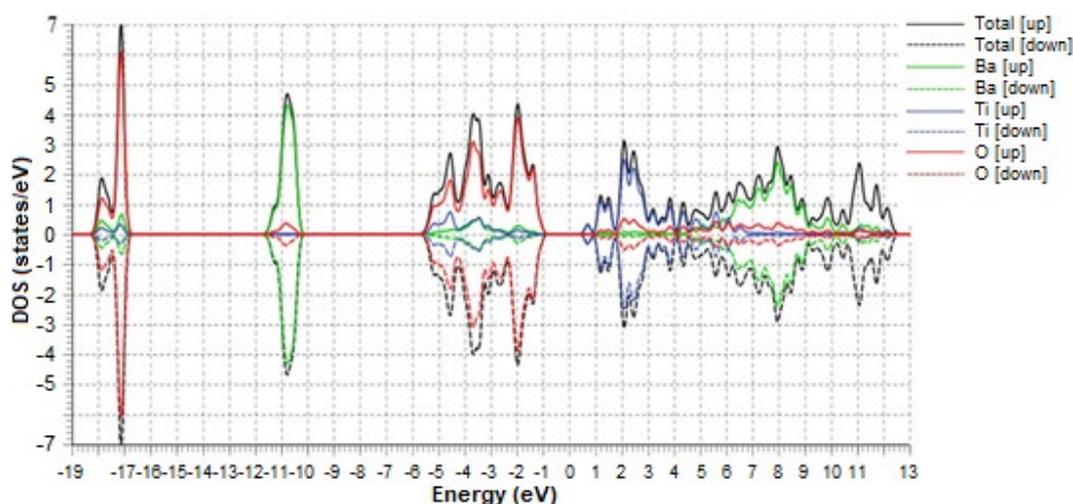
Fig 4. The total density of state (DOS) for cubic BaTiO₃

indicates that some electrons moved from the valence band of the O 2p orbital to the conduction band of Ti 3d and hybridized to form a covalent bond. The Ba state was not influenced by the valence band even when separated from the other bands. The Ba and O states were much larger than the O and Ti states in DOS, which indicates that the Ba–O interaction takes on an ionic character, while the Ti–O interaction takes on a covalent character.

Thermal Characteristics and Electrochemical Properties

Thermal analysis can be used to explain the process of forming barium titanate from its precursors. Theoretically, the formation of $BaTiO_3$ from $Ba(OH)_2$ and TiO_2 precursors will release 7.17% w/w H_2O molecules so that the $BaTiO_3$ material quantity after a water loss is 92.83% w/w. The study of thermal analysis using TG/DTA showed that the percentage loss of weight at 1000 °C by 8% (airflow) and 6.7% (oxygen flow) were in line with theoretical calculations (Fig. 5(a) and 5(b)). The weight loss occurred slowly until reaching a temperature of 650 °C and then increased sharply until reaching the temperature of 950 °C.

The temperature achieved for weight loss acceleration in the airflow was lower than that of the oxygen flow, indicating that airflow can accelerate $BaTiO_3$ formation. This phenomenon followed the TG-DTA pattern of BTO from $BaCO_3$ and TiO_2 and exhibited that the phase transition temperature during $BaTiO_3$ formation will be from 650 °C to 950 °C [30].

Endothermic peaks appeared in a TG-DTA pattern, which indicates a phase change during the formation of $BaTiO_3$. In the airflow, phase transition more frequently occurs, which is possible due to the effects of the chemical components contained in the air, such as N_2, O_2, CO_2, and CO. Ba_2TiO_4 is a possible phase, which occurs due to the reaction between $BaTiO_3$ and $BaCO_3$. This phase will react again with TiO_2 to form $BaTiO_3$ [30]. Endothermic peaks in oxygen flow occur at 750 °C and 900 °C, with sharper characters than airflow. An endothermic DTA peak above 800 °C was associated with CO_2 release due to a reaction between $BaCO_3$ and $BaTiO_3$ to form Ba_2TiO_4. On the other hand, water released in the formation of $BaTiO_3$ from the $Ba(OH)_2$ and TiO_2 precursors requires high temperatures, indicating a strong OH chemisorption in the lattice perovskite [31].

The voltammogram of $BaTiO_3$ indicated an irreversible redox system in the alkaline medium (Fig. 6(a)). A reduction peak appeared at -0.4 V vs. Ag/AgCl, and an oxidation peak appeared at 0.6 V vs. Ag/AgCl, indicating the behavior of Ti^{3+}/Ti^{4+} redox on an electrode surface. On the other hand, the redox system of the $BaTiO_3$ electrode surface caused an oxygen evolution/reduction reaction (OER/ORR) and a hydrogen evolution reaction (HER). Positive potential is the OER/ORR region, while the negative potential is the HER region. The current at a positive potential is higher than negative potential indicating that $BaTiO_3$ is more active as an OER/ORR electrocatalyst. The OER/ORR
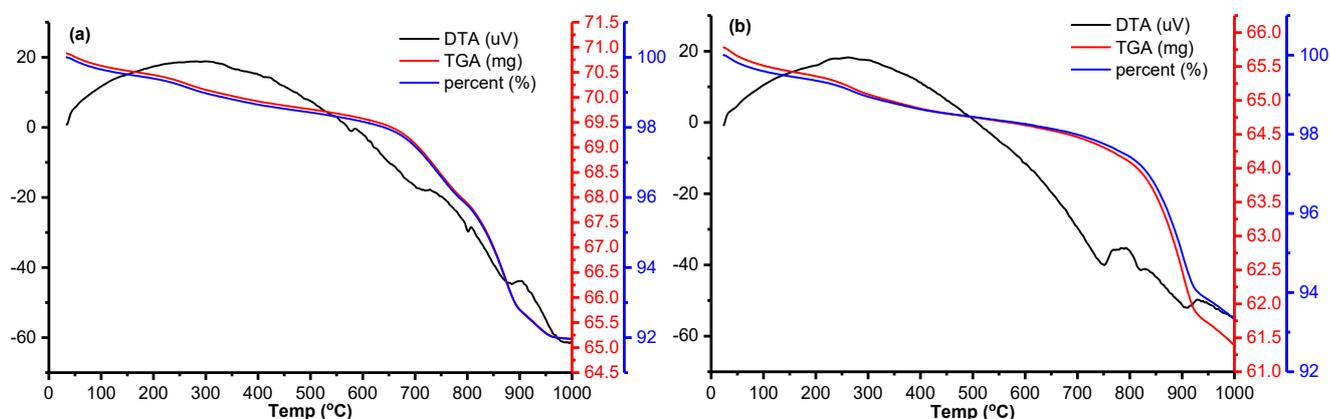
Fig 5. The TG-DTA pattern of the product resulted from low pressure hydrothermal from $Ba(OH)_2$ and TiO_2 before sintering using (A) airflow and (B) oxygen flow
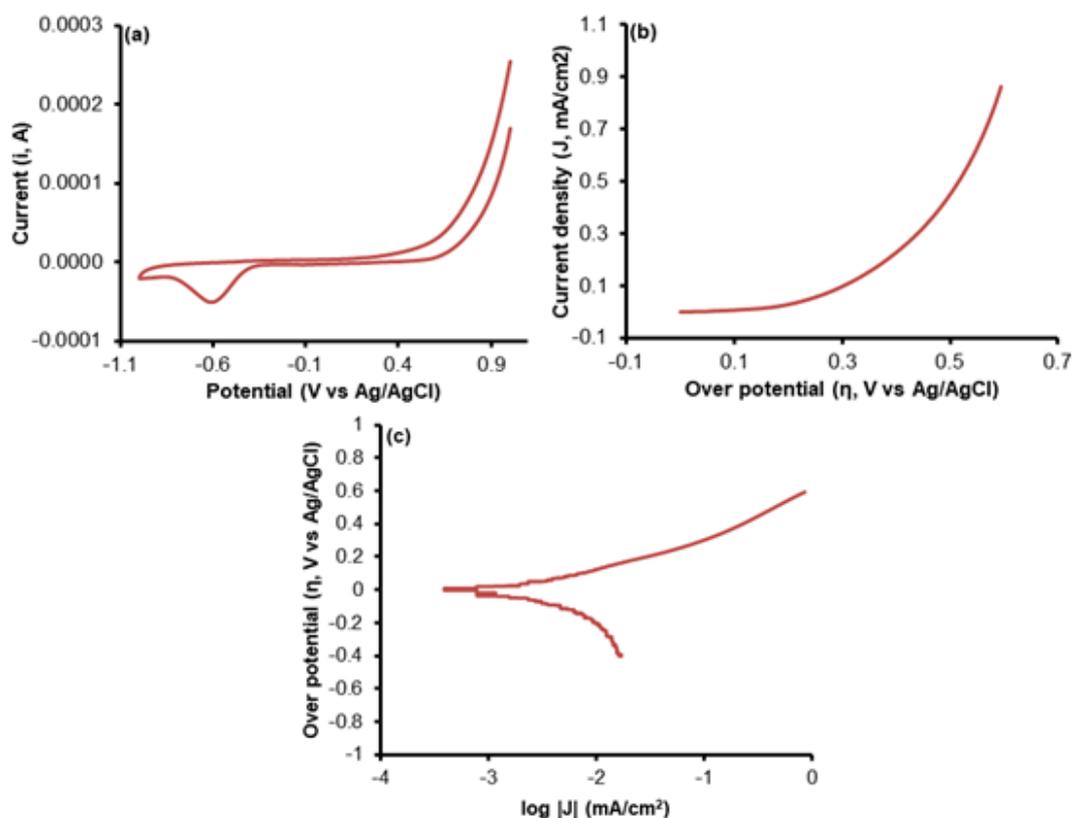
Fig 6. Cyclic voltammogram (a), Polarization plot (b), and Tafel plot (c) of BaTiO$_3$ was produced through sintering at 800 °C during 4 h in 1 M NaOH solution

bifunctional electrocatalyst of BaTiO$_3$ has been studied previously [32] due to the oxygen vacancy of BaTiO$_3$ that changes its crystal structure from cubic to hexagonal. Mechanistic of OER, ORR, and HER are initiated via OH adsorption on the Ti atom, the formation of the O–O bond, and O$_2^{2-}$/$^-$OH exchange. The OER/ORR mechanism of the perovskite has also been previously studied, and a proposed mechanism of OER in an alkaline medium is as follows:

M + $^-$OH → MOH
MOH + $^-$OH → MO + H$_2$O$_{(l)}$
2MO → 2M + O$_{2(g)}$
MO + $^-$OH → MOOH + e$^-$
MOOH + $^-$OH → M + O$_{2(g)}$ + H$_2$O$_{(l)}$
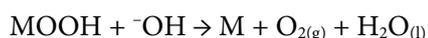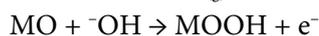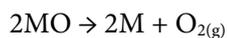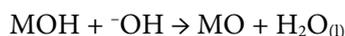
Good electrocatalyst was indicated by Tafel slope value and also may provide insightful information about the OER mechanism. Suen et al. [33] was reviewed various OER mechanisms that correlated with Tafel slope value. Tafel slope value can be linked to the rate-determining step and implicates to some pattern may exist. The same rate-determining steps could have several values of Tafel slope, dependent on different coverage degree of intermediate. OER mechanism included intermediate such oxo, peroxide and superoxide group on surface electrocatalyst.

The OER ability of BaTiO$_3$ can be attributed to the electron configuration system of the Ti atom, in which the d orbitals of Ti are not filled (d^0), so it is possible to interact with more reactive ligands, such as $^-$OH at the initial stage. Based on Hard-Soft Acid Base (HSAB) theory, The Ti ion is categorized as a hard acid, while O^{2-} and $^-$OH are categorized as hard bases. $^-$OH ions are preferred for interacting with Ti compared to O$_2$ ions due to their having a larger degree of basicity. To study the OER mechanism of BaTiO$_3$, the calculation of reaction Gibbs free energy using MMFF-based molecular mechanics was calculated (Fig. 7). The energy profile showed that the OOH stage is the rate

250

Indones. J. Chem., 2022, 22 (1), 242 - 252
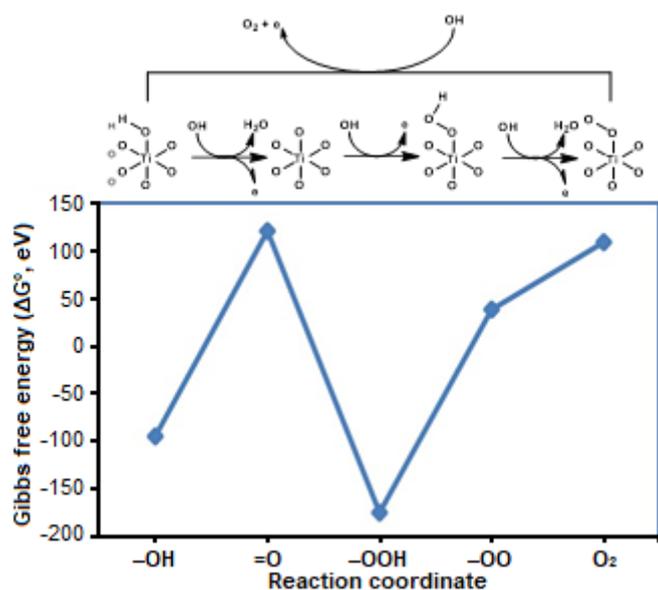
Fig 7. Profile of Gibbs Free Energy in oxygen evolution reaction

determining step, allowing for oxygen evolution in the base medium. The calculation of Gibbs free energy in Fig. 7 was used a mechanism of OER proposed by Hong et al. [34] for perovskite surface.

CONCLUSION

The hydrothermal technique of low-pressure systems followed by sintering at 600, 700, and 800 °C can be used to synthesize $BaTiO_3$ with $Ba(OH)_2$ and TiO_2 precursors. Sintering temperatures of 600 and 700 °C still contain $BaCO_3$ impurities sourced from distilled water and air. The crystal size of $BaTiO_3$ ranged from 82 to 198 nm based on the Williamson-Hall equation with strains from 0.27 to 0.68%. $BaTiO_3$ crystal growth following lattice diffusion is controlled by pore size based on the exponent value of 2-2.5. The band structure of cubic $BaTiO_3$ exhibited an indirect band from the M to Γ band of about 1.75 eV and a direct bandgap of about 1.9 eV at Γ to Γ. The density of state (DOS) indicated the covalent character on the Ti‒O interaction and the ionic character on the Ba‒O interaction. Electrochemical measurements indicated that $BaTiO_3$ has OER electrocatalytic capabilities in an alkaline medium. The purified cubic $BaTiO_3$ offers potential application in electrocatalyst for energy storage and conversion as an electrode for batteries, water splitting systems, and regenerative fuel cells.

REFERENCES

[1] Chen, T., Meng, J., Wu, S., Pei, J., Lin, Q., Wei, X., Li, J., and Zhang, Z., 2018, Room temperature synthesized $BaTiO_3$ for photocatalytic hydrogen evolution, *J. Alloys Compd.*, 754, 184–189.

[2] Artrith, N., Sailuam, W., Limpijumnong, S., and Kolpak, A.M., 2016, Reduced overpotentials for electrocatalytic water splitting over Fe-and Ni-modified $BaTiO_3$, *Phys. Chem. Chem. Phys.,* 18 (42), 29561–29570.

[3] Kudłacik-Kramarczyk, S., Drabczyk, A., Głąb, M., Dulian, P., Bogucki, R., Miernik, K., Sobczak-Kupiec, A., and Tyliszczak, B., 2020, Mechanochemical synthesis of $BaTiO_3$ powders and evaluation of their acrylic dispersions, *Materials*, 13 (15), 3275.

[4] Gaikwad, A.S., More, S.S., Kathare, R.V., Mane, M.L., Borade, R.B., Vijapure, Y.A., and Kadam, A.B., 2018, Barium titanate ($BaTiO_3$) synthesized by sol-gel auto-combustion method, *Int. Res. J. Sci. Eng.*, A5, 41–44.

[5] Wang, W., Cao, L., Liu, W., Su, G., and Zhang, W., 2013, Low-temperature synthesis of $BaTiO_3$ powders by the sol–gel-hydrothermal method, *Ceram. Int.*, 39 (6), 7127–7134.

[6] Wu, Y.T., Wang, X.F., Yu, C.L., and Li, E.Y., 2012, Preparation and characterization of barium titanate ($BaTiO_3$) nano-powders by pechini sol-gel method, *Mater. Manuf. Processes*, 27 (12), 1329–1333.

[7] Zanfir, A.V., Voicu, G., Jinga, S.I., Vasile, E., and Ionita, V., 2016, Low-temperature synthesis of $BaTiO_3$ nanopowders, *Ceram. Int.*, 42 (1), 1672–1678.

[8] Zhang, B., Jin, H., Liu, X., Guo, X., He, G., and Yang, S., 2019, The formation and application of submicron spherical $BaTiO_3$ particles for the diffusion layer of medical dry films, *Crystals*, 9 (11), 594.

[9] Gao, Y., Shvartsman, V.V., Elsukova, A., and Lupascu, D.C., 2012, Low-temperature synthesis of

crystalline BaTiO₃ nanoparticles by one-step "organosol"-precipitation, *J. Mater. Chem.*, 22 (34), 17573–17583.

[10] Bowland, C.C., and Sodano, H.A., 2017, Hydrothermal synthesis of tetragonal phase BaTiO₃ on carbon fiber with enhanced electromechanical coupling, *J. Mater. Sci.*, 52 (13), 7893–7906.

[11] Li, J., Inukai, K., Tsuruta, A., Takahashi, Y., and Shin, W., 2017, synthesis of highly disperse tetragonal BaTiO₃ nanoparticles with core–shell by a hydrothermal method, *J. Asian Ceram. Soc.*, 5 (4), 444–451.

[12] Yan, C., Zou, L., Xue, D., Xu, J., and Liu, M., 2008, Chemical tuning polymorphology of functional materials by hydrothermal and solvothermal reactions, *J. Mater. Sci.*, 43 (7), 2263–2269.

[13] Khan, M., Mishra, A., Shukla, J., and Sharma, P., 2019, X-ray analysis of BaTiO₃ ceramics by Williamson-Hall and size strain plot methods, *AIP Conf. Proc.*, 2100, 020138.

[14] Yun, H.S., Yun, B.G., Shin, S.Y., Jeong, D.Y., and Cho, N.H., 2021, Crystallization kinetics in BaTiO₃ synthesis from hydrate precursors via microwave-assisted heat treatment, *Nanomaterials*, 11 (3), 754.

[15] Usher, T.M., Kavey, B., Caruntu, G., and Page, K., 2020, Effect of BaCO₃ impurities on the structure of BaTiO₃ nanocrystals: Implications for multilayer ceramic capacitors, *ACS Appl. Nano Mater.*, 3 (10), 9715–9723.

[16] Viviani, M., Buscaglia, M.T., Testino, A., Buscaglia, V., Bowen, P., and Nanni, P., 2003, The influence of concentration on the formation of BaTiO₃ by direct reaction of TiCl₄ with Ba(OH)₂ in aqueous solution, *J. Eur. Ceram. Soc.*, 23 (9), 1383–1390.

[17] Pasuk, I., Neațu, F., Neațu, Ș., Florea, M., Istrate, C.M., Pintilie, I., and Pintilie, L., 2021, Structural details of BaTiO₃ nano-powders deduced from the anisotropic XRD peak broadening, *Nanomaterials*, 11 (5), 1121.

[18] Lee, H.W., Moon, S., Choi, C.H., and Kim, D.K., 2012, Synthesis and size control of tetragonal barium titanate nanopowders by facile solvothermal method, *J. Am. Ceram. Soc.*, 95 (8), 2429–2434.

[19] Li, M., Gu, L., Li, T., Hao, S., Tan, F., Chen, D., Zhu, D., Xu, Y., Sun, C., and Yang, Z., 2020, TiO₂-seeded hydrothermal growth of spherical BaTiO₃ nanocrystals for capacitor energy-storage application, *Crystals*, 10 (3), 202.

[20] Ahn, K.H., Lee, Y.H., Kim, M., Lee, H.S., Youn, Y.S., Kim, J., and Lee, Y.W., 2013, Effects of surface area of titanium dioxide precursors on the hydrothermal synthesis of barium titanate by dissolution–precipitation, *Ind. Eng. Chem. Res.*, 52 (37), 13370–13376.

[21] Habib, A., Stelzer, N., Angerer, P., and Haubner, R., 2011, Effect of temperature and time on solvothermal synthesis of tetragonal BaTiO₃, *Bull. Mater. Sci.*, 34 (1), 19–23.

[22] Wu, M., Long, J., Wang, G., Huang, A., Luo, Y., Feng, S., and Xu, R., 1999, Hydrothermal synthesis of tetragonal barium titanate from barium hydroxide and titanium dioxide under moderate conditions, *J. Am. Ceram. Soc.*, 82 (11), 3254–3256.

[23] Maxim, F., Ferreira, P., Vilarinho, P.M., Aimable, A., and Bowen, P., 2010, Additive-assisted aqueous synthesis of BaTiO₃ nanopowders, *Cryst. Growth Des.*, 10 (9), 3996–4004.

[24] Ortiz-Landeros, J., Gómez-Yáñez, C., López-Juárez, R., Dávalos-Velasco, I., and Pfeiffer, H., 2012, Synthesis of advanced ceramics by hydrothermal crystallization and modified related methods, *J. Adv. Ceram.*, 1 (3), 204–220.

[25] Fu, F., Zhai, J., Xu, Z., Shen, B., and Yao, X., 2014, Grain growth kinetics of textured-BaTiO₃ ceramics, *Bull. Mater. Sci.*, 37 (4), 779–787.

[26] Kambale, K.R., Kulkarni, A.R., and Venkataramani, N., 2014, Grain growth kinetics of barium titanate synthesized using conventional solid state reaction route, *Ceram. Int.*, 40 (1), 667–673.

[27] Osman, K.I., 2011, Synthesis and Characterization of BaTiO₃ Ferroelectric Material, *Dissertation*, Faculty of Engineering, Cairo University.

[28] Rohj, R.K., Hossain, A., Mahadevan, P., and Sarma, D.D., 2021, Band gap reduction in ferroelectric BaTiO₃ through heterovalent Cu-Te co-doping for visible-light photocatalysis, *Front. Chem.*, 9, 682979.

[29] Taib, M.F.M., Hussin, N.H., Samat, M.H., Hassan, O.H., and Yahya, M.Z.A., 2016, Structural, electronic and optical properties of $BaTiO_3$ and $BaFeO_3$ from first principles LDA+U study, *Int. J. Electroact. Mater,* 4, 14–17.

[30] Gomez-Yañez, C., Benitez, C., and Balmori-Ramirez, H., 2000, Mechanical activation of the synthesis reaction of $BaTiO_3$ from a mixture of $BaCO_3$ and TiO_2 powders, *Ceram. Int.*, 26 (3), 271–277.

[31] Hennings, D., and Schreinemacher, S., 1992, characterization of hydrothermal barium titanate, *J. Eur. Ceram. Soc.*, 9 (1), 41–46.

[32] Chen, C.F., King, G., Dickerson, R.M., Papin, P.A., Gupta, S., Kellogg, W.R., and Wu, G., 2015, Oxygen-deficient $BaTiO_{3-x}$ perovskite as an efficient bifunctional oxygen electrocatalyst, *Nano Energy*, 13, 423–432.

[33] Suen, N.T., Hung, S.F., Quan, Q., Zhang, N., Xu, Y.J., and Chen, H.M., 2017, Electrocatalysis for the oxygen evolution reaction: recent development and future perspectives, *Chem. Soc. Rev.*, 46 (2), 337–365.

[34] Hong, W.T., Risch, M., Stoerzinger, K.A., Grimaud, A., Suntivich, J., and Shao-Horn, Y., 2015, Toward the rational design of non-precious transition metal oxides for oxygen electrocatalysis, *Energy Environ. Sci.*, 8 (5), 1404–1427.